



Synthesis of hollow NiO nanostructures and their application for supercapacitor electrode

Xiaoshuang Wang¹ · Ling Chen¹ · Fei Li¹ · Shuoqing Zhang¹ · Xiangcheng Chen¹ · Juanjuan Yin¹

Received: 14 July 2018 / Revised: 8 October 2018 / Accepted: 13 October 2018 / Published online: 20 October 2018
© Springer-Verlag GmbH Germany, part of Springer Nature 2018

Abstract

Hollow NiO nanostructures were fabricated by calcining Ni(OH)₂ precursors built on the basis of Cu₂O templates. The structures and morphology of the products were characterized using X-ray diffraction, scanning electron microscopy, and transmission electron microscopy. As the temperature rose from 250 to 550 °C, the products showed stable cubic structures with the lengths about 600 nm of a side at first, then some products deformed into cylinders and debris is generated, and the NiO nanostructures collapsed at 550 °C. Electrochemical test results from cyclic voltammetry, electrochemical impedance spectroscopy, and galvanostatic charging–discharging demonstrated that the sample synthesized at 450 °C showed better electrochemical properties. The hollow NiO nanostructures obtained at 450 °C delivered a capacitance of 1200 F g⁻¹ at 1 A g⁻¹ and displayed good rate capability with a large capacitance of 1010 F g⁻¹ at 5 A g⁻¹. After improving the cycle stability, it will exhibit a more admirable prospect of application.

Keywords Nickel oxide · Nanostructures · Pseudocapacitor · Specific capacitance

Introduction

Due to the rapid consumption of fossil fuels and continuous deterioration of the environment, the clean energy technology has emerged as a key challenge to energy storage. Supercapacitors, also known as electrochemical supercapacitors, have received a number of attention owing to their various merits, including long cycle life, safety, no memory effect, and high power density [1–4]. Different charge storage mechanisms divide supercapacitors into three categories namely electric double layer capacitors (EDLCs), pseudocapacitors, and hybrid electrochemical capacitors. EDLCs store charges at the interface between electrode and electrolyte through ion absorption/desorption while pseudocapacitors store charges at the surface of electroactive materials via fast and reversible superficial Faradaic redox reactions. EDLCs' application is hampered by lower practical

energy density [5–8]. However, the capacitance of pseudocapacitors is 3–4 times higher than that of EDLCs because redox reactions between electrolyte ions and electroactive materials can store more charges in the capacitors. Typical electrode materials of pseudocapacitors mainly include transition metal oxides and conducting polymers. Among the transition metal oxides, RuO₂ (specific capacitance > 600 F g⁻¹) has been applied in the military field successfully. Even so, the high cost and toxicity restrict its commercialization [9]. Hence, tremendous efforts have been paid to study other metal oxides such as MnO₂, Co₃O₄, Fe₃O₄, and NiO in order to develop cheap and environmentally friendly electrode materials [10–18].

Among the alternative candidates, cost-effective NiO has been recognized as one of the promising materials for pseudocapacitors owing to its outstanding theoretical specific capacitance (3750 F g⁻¹) and high chemical and thermal stability [19–21]. In general, metal oxides with larger surface area can devote larger specific capacitance because of more Faradic active sites. Therefore, the morphology of electroactive materials has a great influence on their electrochemical performance. To date, numerous researchers have reported [22–28] the synthesis of NiO with different structures, including nano/microspheres [27], nanosheets [29, 30], and nanofibers [31] via various methods such as sol–gel

✉ Ling Chen
hhchen@ysu.edu.cn

¹ Hebei Key Laboratory of Applied Chemistry, College of Environmental and Chemical Engineering, Yanshan University, Qinhuangdao 066004, China

method [32], anodization method [33], solvothermal/hydrothermal techniques [34, 35], and hard template methods [36]. For instance, Cai et al. [37] synthesized daisy-like α -Ni(OH)₂ via hydrothermal method, after being calcined at 600 °C, the obtained NiO showed high specific capacitance of 517 mAh g⁻¹. Meng et al. [38] reported NiO prepared by electrodeposition technique exhibited the maximum specific capacitance of 3144 F g⁻¹ at 5 mA cm⁻². Using petals of plants as raw materials, Kundu [39] prepared flower-like NiO which could deliver specific capacitance of 752 F g⁻¹ at 1 A g⁻¹, no obvious decay occurred after 5000 cycles at 10 A g⁻¹. Although hollow cubic Ni(OH)₂ with great performance has been prepared [2], preparation of NiO nanostructures based on the Ni(OH)₂ hollow nanoboxes has not been reported.

Although there are many facile methods for the synthesis of NiO, such as hydrothermal method, electrodeposition method and so on, the template method is more convenient to maintain controllable structure of NiO. NiO with proper structure can improve the contact between electrolyte and active materials, which is expected to deliver higher capacitance. In this paper, we synthesized hollow cubic Ni(OH)₂ precursors based on Cu₂O templates, then the precursors were calcined to hollow NiO nanostructures consisting mainly of cubes. Electrochemistry data demonstrate that the NiO nanostructures gained at 450 °C deliver the highest specific capacitance of 1200 F g⁻¹ at 1 A g⁻¹ and exhibit an excellent capacitance of 1010 F g⁻¹ at a high rate of 5 A g⁻¹, which indicates its promising application in supercapacitors.

Experiments

Synthesis of NiO nanostructures

Cu₂O templates were synthesized as follows. One hundred-milliliter NaOH (2 mol L⁻¹) solution was added dropwise into 100 mL CuCl₂ (0.01 mol L⁻¹) solution, the mixture was heated at 55 °C for 30 min under constant magnetic stirring, then 10 mL ascorbic acid solution was added. The solution became dark red and aged for 180 min. The precipitant was purified by washing and centrifugation for several times. Cu₂O templates were generated after dried.

Synthesis of the precursors started with mixing 0.1 g Cu₂O, 0.034 g Ni(NO₃)₂ and 3.33 g surfactant (Hexadecyl trimethyl ammonium Bromide (CTAB) or polyvinyl pyrrolidone (PVP)) in 100 mL alcohol and deionized water solution (V_{alcohol}: V_{water} = 1:1) while stirring. Subsequently, 40 mL Na₂S₂O₃ (1 mol L⁻¹) was added. The mixture was stirred for 10 min to form precursors. The as-prepared precursors were cleaned by repeated washing and centrifuging and then were converted by calcining at 250, 350, 450, and 550 °C for 3 h in a muffle furnace.

Characterization

The samples were characterized by scanning electron microscope (SEM, Carl Zeiss, SUPRA55) and transmission electron microscope (TEM, Hitachi HT-7700). X-ray diffraction (XRD) patterns were collected on a Rigaku Lab X-ray diffractometer operated at 40 Kv using Cu K α radiation at a scan rate of 5 °/min. The thermogravimetry analysis (TGA) was performed in air with a heating rate of 10 °C min⁻¹.

Electrochemical measurements

Electrochemical performance of the samples was tested by cycle voltammetry (CV, CHI660e electrochemical workstation, Shanghai CH instrument, China), galvanostatic charge-discharge (GCD, Neware battery testing system, Shenzhen Neware instrument, China) and Electrochemical impedance spectroscopy (EIS, CHI660e electrochemical workstation, Shanghai CH instrument, China). All tests were performed in a three-electrode system, in which Platinum gauze electrode and Hg/HgO electrode were used as the counter and the reference electrode, respectively. The working electrode was comprised of 80 wt% of active materials, 15 wt% of acetylene black, and 5 wt% of polytetrafluoroethylene (PTFE) binder. The electrolyte was 6 M KOH. CV data were collected between 0 and 0.6 V at a scan rate of 2 mV s⁻¹ and GCD tests were conducted in the potential range of 0–0.5 V (the voltage window is the optimal result). EIS tests were performed between the frequency range of 10⁻² and 10⁵ Hz at a 5-mV amplitude referring to open circuit potential. The mass-specific capacitances were calculated using the following equation [40],

$$C = It/V$$

where I is the discharging current density (A g⁻¹), t is the discharging time (s), and V is the discharging potential range (V), respectively.

Results and discussion

The crystal structures of the precursor and calcination products were verified by XRD characterization, as shown in Fig. 1. Diffraction peaks of the precursor are broad and smooth, which agrees well with 3Ni(OH)₂·2H₂O (JCPDS 22–0444). After annealed at 250 °C, diffraction peaks of the calcination product still almost correspond to 3Ni(OH)₂·2H₂O, indicating that this calcination temperature removed merely unbound water from the precursor and made no dehydration effect on the bound water. As the calcination temperature rose to 350 °C, the precursor began to be stripped of some water and converted to Ni(OH)₂·0.75H₂O (JCPDS 38-0715). It is

worth noting that the peak corresponding to the (200) plane of NiO has been observed. When the precursor was annealed at 450 °C, the appearing peaks at the positions of $2\theta = 43.2$, and 62.9° correspond to the (200), and (220) planes of the NiO (JCPDS 47–1049), confirming the presence of NiO nanostructures. Besides, the (012) and (015) planes imply a minute quantity of $\text{Ni}(\text{OH})_2 \cdot 0.75\text{H}_2\text{O}$. Intensities of diffraction peaks increased while increasing the calcination temperature to 550 °C, the precursor was also converted into NiO. As observed, some extra diffraction peaks around 20° occurred when the calcination temperature increased to 550 °C (red circle part in Fig. 1). These diffraction peaks may correlate the split products of residual PVP that cracked at the elevated temperature. Comparing the XRD patterns, we can find that part of diffraction peaks are not obvious, which is due to the preferred orientation growth of crystal in (111) and (200) planes and the weak crystallization degree.

TGA was used to analysis the detailed effect of calcination temperatures (Fig. 2). The curves of precursor ($3\text{Ni}(\text{OH})_2 \cdot 2\text{H}_2\text{O}$) and calcination products at 250 °C ($3\text{Ni}(\text{OH})_2 \cdot 2\text{H}_2\text{O}$) and 350 °C ($\text{Ni}(\text{OH})_2 \cdot 0.75\text{H}_2\text{O}$) show similar two-step weight loss at 100 and 400 °C, which corresponds to the removal of unbound water and the elimination of bound water or decomposition of intercalated surfactant molecules, respectively. In addition, the weight loss of the above three samples after 400 °C also corresponds to the decomposition of $\text{Ni}(\text{OH})_2$. It is obvious that the weight loss of the product obtained at 450 °C (NiO) mainly occurs at 530 °C, which is mainly attributed to the collapse of NiO cubes, accompanied by decomposition of a minute quantity of inner unconverted $\text{Ni}(\text{OH})_2$ simultaneously. However, the above phenomenon is not presented in the product obtained at 550 °C because the collapse process has already occurred during the period of calcination. The total mass loss decreases with the increase of calcination

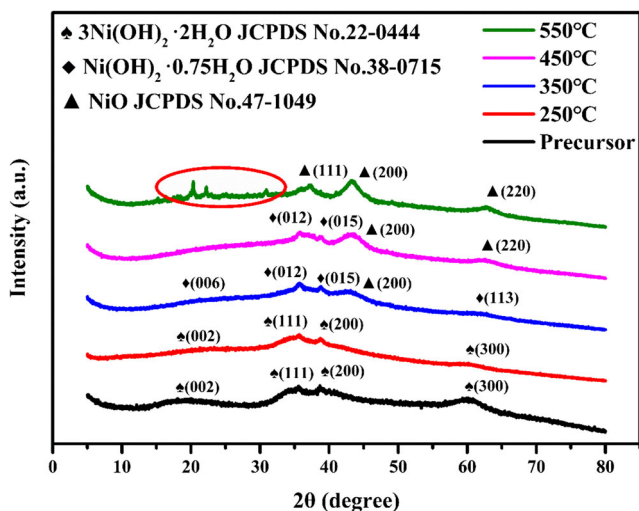


Fig. 1 XRD patterns of the as-prepared precursor and the calcination products

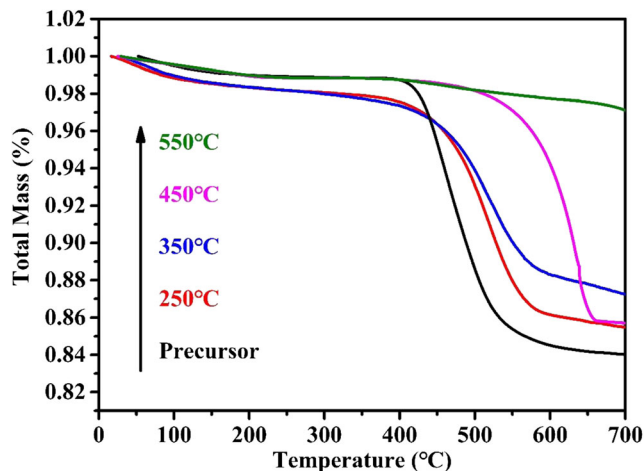


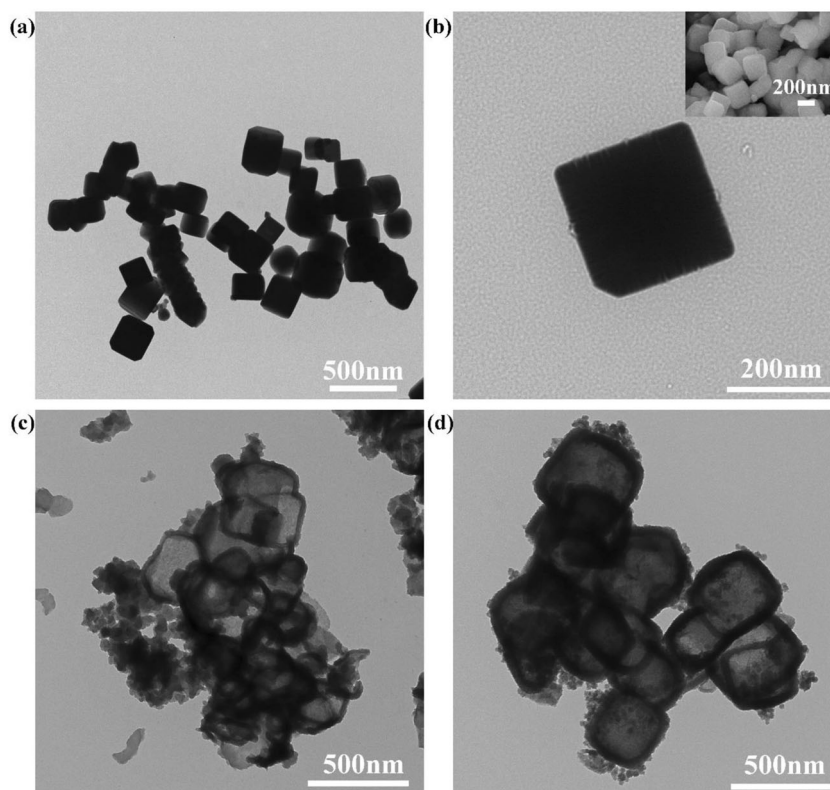
Fig. 2 TGA curves of the as-prepared precursor and the calcination products

temperature, because different components of calcination products contain different amounts of water molecules and impurities, which can be seen from the respective chemical formula deduced from XRD patterns (Fig. 1).

The nanostructures of Cu_2O templates and the precursor were revealed using TEM and SEM. As posted in Fig. 3a, b, well-distributed Cu_2O cubes with sizes of 200 nm can be observed apparently. In order to achieve a uniform and regular hollow cube-shaped precursor, we used CTAB or PVP to assist the preparation process, respectively. The surfactant acts as a soft template to reduce the surface free energy of crystal nuclei and regulates the growth of crystals in different directions [41]. The former product (Fig. 3c) undergoes a partial collapse, while the latter (Fig. 3d) exhibits a stable hollow cube-shaped structure. TEM images (Fig. 3c, d) reveal that the PVP helps the precursor to retain the original cubic structure of Cu_2O more efficiently (Fig. 3a, b). With respect to the anionic CTAB, the non-ionic PVP probably has well control on the Ostwald ripening process, so that the $3\text{Ni}(\text{OH})_2 \cdot 2\text{H}_2\text{O}$ nanostructures whose thickness is around 75 nm retain the shape and size of the Cu_2O template. The average size of the cubic precursor is about 500 nm, which can provide the high specific surface and low-resistant ion diffusion pathways and deliver high specific capacitance.

After calcined at different temperatures, the hollow box-shaped precursor converted into hollow cube-shaped products successfully. Figure 4 shows SEM images of the precursor and products. It is clear that the internal structure of the cube-shaped products can be observed, which are marked by red rectangles on the images (Fig. 4b, d, f, h). However, the cubes begin to collapse into nanocylinders with the temperature rising to 550 °C. Combining the SEM results with XRD analysis, we can conclude that the component and shape of the calcination product at 250 °C did not change and remained consistent with the precursor (Fig. 4a, b, c, d). The component of the product gained at 350 °C changed with dehydration, but it still held

Fig. 3 TEM images of Cu_2O templates observed at low magnification (a) or high magnification (b), and the precursor synthesized using CTAB (c) or PVP (d), a SEM image of Cu_2O is in the top right corner of (b)

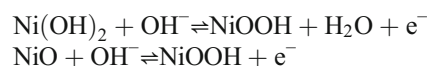


hollow cubic nanostructures (Fig. 4e, f). During the calcination process at 450 °C and 550 °C, the precursor was completely converted to NiO nanostructures (Fig. 4g, h, i, j). Unfortunately, the original hollow cubic structure was destroyed at 550 °C. At the same time, some irregularly shaped debris that may attribute to the cleavage products of PVP appeared among NiO nanostructures (Fig. 4i, j), which lead to the emergence of extra diffractions of a new phase in XRD.

The elemental mapping images (Fig. 5a, b) display that O, Ni, Cu, and S distribute uniformly within the structure. Apparently, Ni accounts for a larger proportion of the calcination product obtained at 450 °C than the precursor, which is mainly due to the removal of large amounts of hydrogen and oxygen elements through the calcination process. Furthermore, the summary of quant results also corroborate the chemical formulas (Fig. 5c). With different calcination temperatures, the ratios of oxygen to nickel of precursors and calcination products are 2.8, 2.7, 2.8, 1.3, and 1.2, which gradually approach the theoretical ratio (1.0) of oxygen to nickel in NiO. Residual Cu and S elements just account for a small proportion, which originates from Cu_2O and $\text{Na}_2\text{S}_2\text{O}_3$, respectively.

The electrochemical performance of the precursor and calcination products synthesized at different temperatures was compared by mean of CV at 2 mV s^{-1} and shown in Fig. 6a. Every CV curve exhibits well-defined symmetric redox peaks

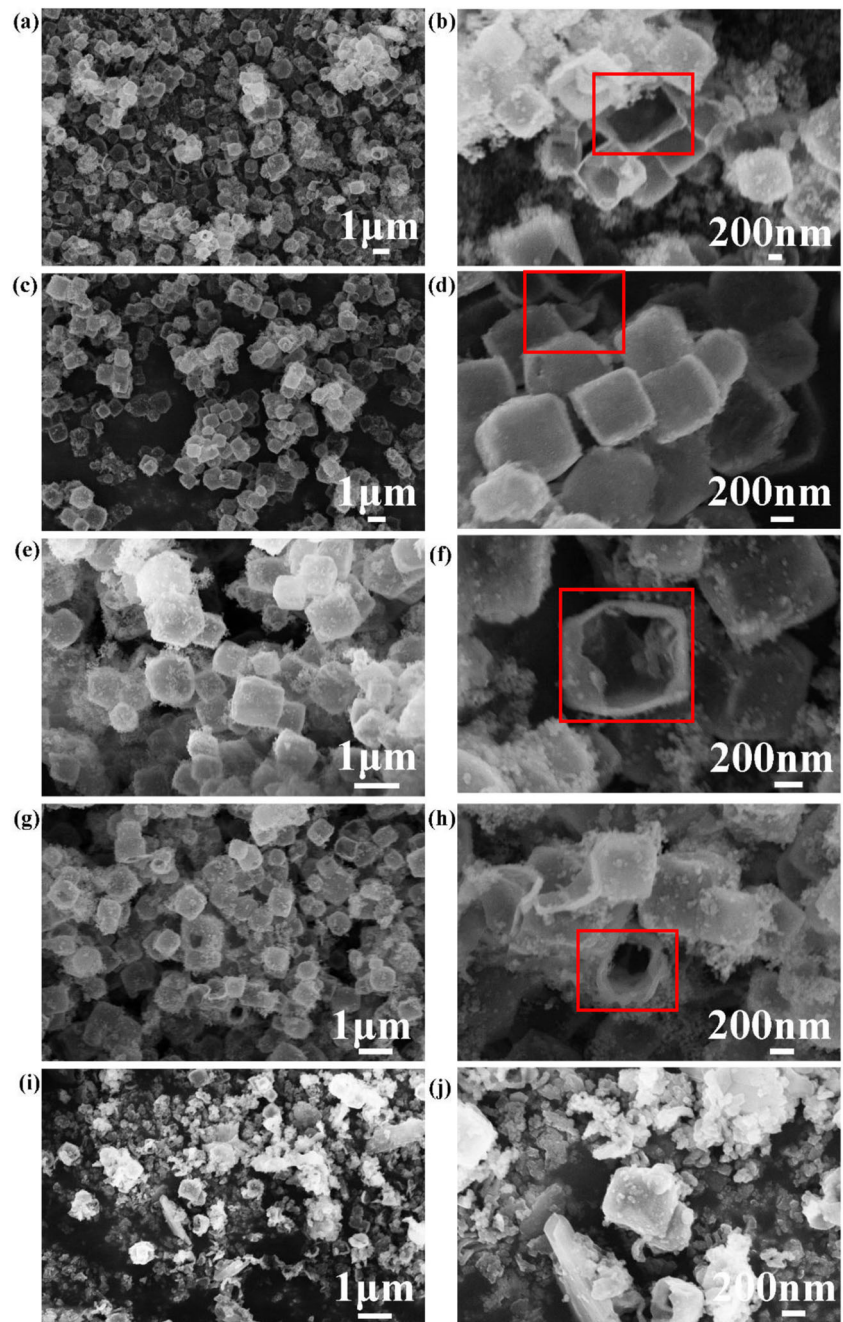
confirming the Faradic nature of the products rather than EDLC whose curve is an ideal rectangular shape. The capacitors of products mainly rely on the charges kept in the host materials through redox reactions on the surface. The surface Faradaic reactions can be expressed as follows:



Peaks observed in a CV curve are in accordance with the change of the valence of the element Ni. Moreover, outlines of peaks of NiO hollow nanostructures obtained at 450 °C are much sharper than the others, from which we can perceive the rapidity of the redox reactions. Meanwhile, minor peak separation (0.18 V) demonstrates decreased electrochemical polarization. Moreover, it is apparent that the hollow NiO nanostructures synthesized at 450 °C occupy the maximum area among the CV curves, which is identified to possess the largest specific capacitance. In addition to the hollow structures which give NiO a sufficient internal space that facilitates the rapid mass transfer dynamics, its large surface area also offers a lot of electrochemically active sites that accelerate the Faradaic redox reactions. Both of the above two points are beneficial to perform a considerable specific capacitance.

Figure 6b presents the charging-discharging curves of the precursor and the calcination products at 1 A g^{-1} . The

Fig. 4 SEM images of the precursor (a, b) and the products synthesized at 250 °C (c, d), 350 °C (e, f), 450 °C (g, h), and 550 °C (i, j)



nonlinear charging–discharging curves demonstrate the feature of pseudocapacitance, which is in agreement with other literature [5]. When comparing the discharge curves, we notice that the discharge time of the NiO nanostructures obtained at 450 °C is the longest among curves of the precursor and samples got at other calcining temperatures, which suggests that NiO nanostructures have great charge storage performance that is far better than the others. By calculation, the precursor and calcination products obtained at 250, 350, 450, and 550 °C show discharge specific capacitance values of 780, 580, 590, 1200, and 380 F g⁻¹, respectively, at 1 A g⁻¹.

The rate capabilities of the samples were examined under different current densities, as shown in Fig. 7a. The curve of the precursor displays an apparent drop while the curves of calcination products are almost horizontal. The precursor retains merely 44.13% of its specific capacitance delivered at 1 A g⁻¹ when the current density increases to 5 A g⁻¹. The specific capacitance of the NiO nanostructures obtained at 450 °C at 1, 2, 3, 4, and 5 A g⁻¹ reaches 1200, 1180, 1150, 1050, and 1010 F g⁻¹, respectively. Besides, the capacitance retention of the calcination products improves from 43.34 to 88.6% gradually with rising calcining temperatures from 250

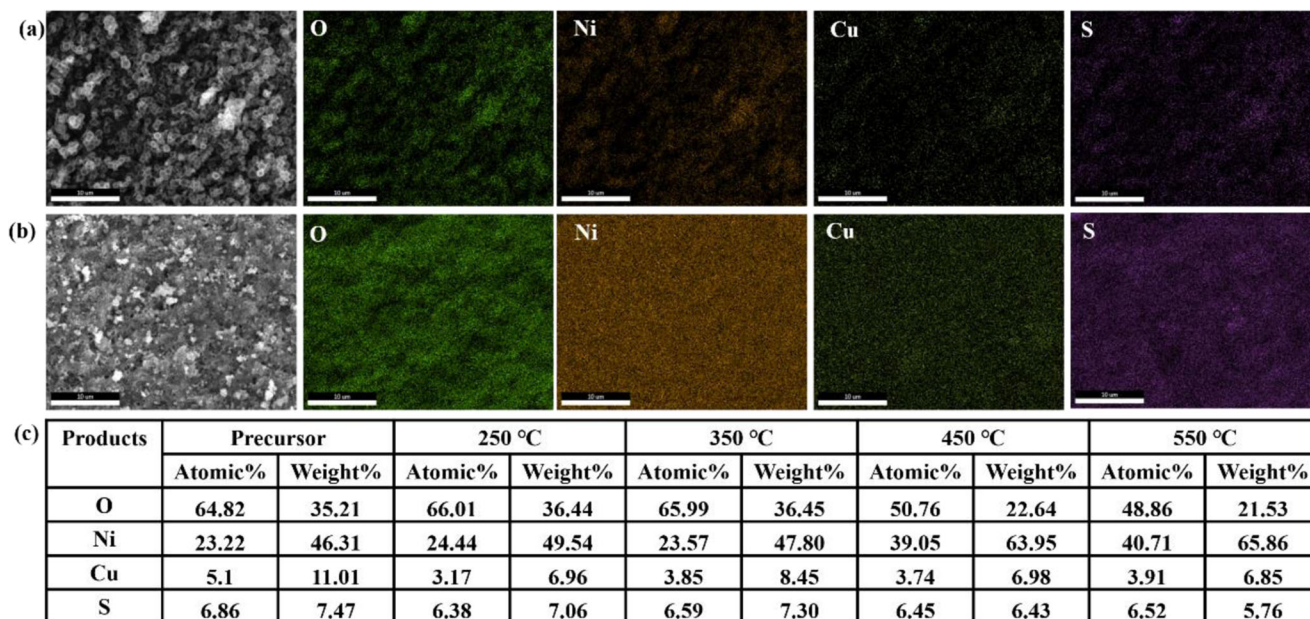


Fig. 5 EDS mapping of O, Ni, Cu and S elemental distribution of the precursor (a) and the calcination product at 450 °C (b) and the summary of quant results (c)

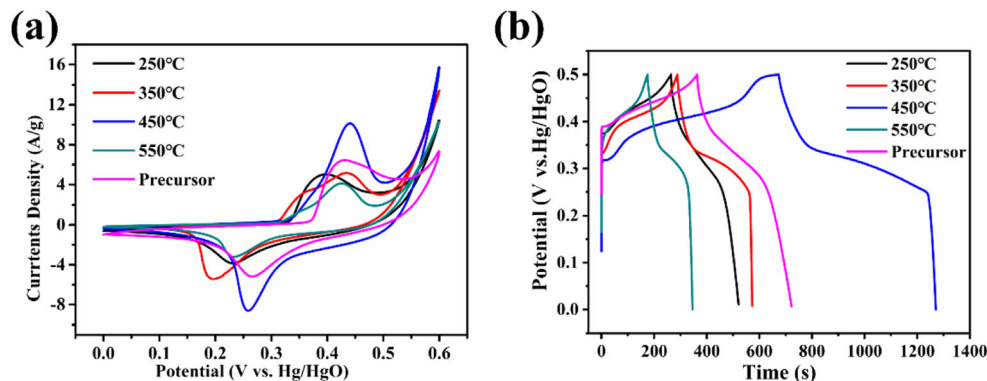
to 450 °C. Nevertheless, the capacitance retention falls to 71.68% at 550 °C. It may be explained by that the NiO nanostructures synthesized at 450 °C maintains the regular hollow cube-shaped structures, as observed in the SEM images (Fig. 4g, h), but the regular nanostructure is destroyed unfortunately into piles of debris at 550 °C (Fig. 4i, j), which reduces the specific surface area of the electroactive materials and exacerbates the resistance of ions diffusion process, thus the electrochemical performance is dented.

Electrochemical impedance spectra of various samples are shown in Fig. 7b. Each curve composes of two parts: the high and low-frequency region. It is obvious that the intercept which is consistent with the ohmic resistance is close to zero for all samples. The semicircle region is related to the charge transfer resistance which reveals Faradaic resistance of the active materials. The straight line in the low-frequency corresponds to Warburg impedance which indicates the ion diffusion rate of the electrolyte within the redox process. As

observed, the other samples have a large charge transfer resistance with the exception of the products obtained at 450 and 550 °C. The EIS curves of these two samples exhibit similar shapes with a negligible semicircle in the high-frequency region and a nearly vertical line in the low-frequency region, which results in excellent electrochemical properties. But it should still be emphasized by the poor performances of the NiO obtained at 550 °C that structure does have a significant influence on the electrochemical properties. It is also necessary to further study the structural changes of active substances during the charging–discharging process in order to find appropriate measures to maintain structural stability and ameliorate electrochemical performance.

Commercial applications of supercapacitors depend largely on the long cycle life. The cycle stability of the samples was investigated at a current density of 2 A g⁻¹, as shown in Fig. 7c. Capacitance retention of 48.7%, 56.5%, 51.9%, 37.4%, and 61.1% for the precursor and the products obtained at

Fig. 6 CV (a) and charging–discharging curves (b) of the precursor and the calcination products synthesized at different calcining temperatures



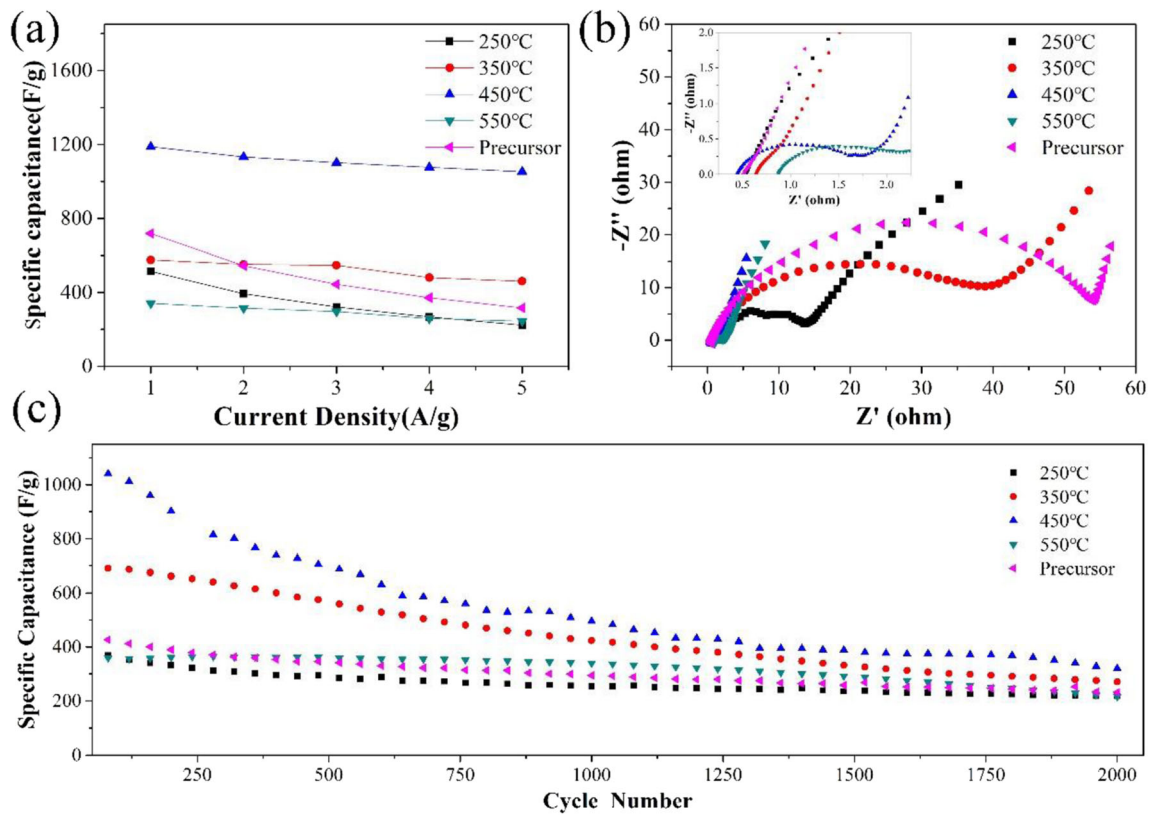


Fig. 7 Rate capabilities (a), electrochemical impedance spectra (b), and cycle numbers (c) of the precursor and the calcination products synthesized at different temperatures

250, 350, 450, and 550 °C are observed after 2000 cycles, respectively. The capacity retention shows a tendency to drop in the first 500 cycles, which may be due to the activation that continuously expands and shrinks the structure of the active materials during the charging-discharging process, then the cycle curves seem to be stable. Although the capacity retention of the NiO nanostructures obtained at 450 °C is the lowest, its capacity is always higher than that of other samples throughout the long cycle test. Besides, referred to the literature results of recent years, NiO nanostructures we synthesized still hold auspicious specific capacitance (see Table 1).

As for the poor cycle stability, we suppose that there are two reasons for it. One is the existence of multiple phases including the primary calcination products, unconverted precursors and residual surfactant molecules in the samples, which could be inferred from XRD patterns and TGA curves. The other is the fast convert rate at 450 °C results in unstable structure of NiO. Meanwhile, the substances at inner cube walls are not converted completely as a result of the insufficient calcination time, which may initiate side reactions during the charge-discharge processes, influencing the cycle stability.

Table 1 Preparation and properties of nickel oxide in pieces of literature

Synthesis method	Specific capacitance	Reference
Liquid phase-separation	794.0 F g ⁻¹ at 1 A g ⁻¹	[42]
Solvothermal method	1386 F g ⁻¹ at 1 A g ⁻¹	[35]
Potentiostatic electrodeposition	667.24 F g ⁻¹ at 5 mV s ⁻¹	[43]
Chemical precipitation	1124 F g ⁻¹ at 2 A g ⁻¹	[44]
Hydrothermal method	170 F g ⁻¹ at 5 A g ⁻¹	[20]
Hydrothermal method	2018 F g ⁻¹ at 2.27 A g ⁻¹	[12]
Ionic layer adsorption and reaction method	783 F g ⁻¹ at 2 mV s ⁻¹	[45]
Electrodeposition method	929 F g ⁻¹ at 1 A g ⁻¹	[46]
Template method	1200 F g ⁻¹ at 1 A g ⁻¹	This work

Conclusions

Hollow NiO nanostructures were synthesized through calcining the precursor at different temperatures. The components and structure of the products changed with calcination temperature, but the structure collapsed at 550 °C, which had an inactive effect on its electrochemical performance. Choosing a right temperature to maintain a good structure is crucial to achieving excellent electrochemical performance. NiO nanostructures prepared at 450 °C can deliver a specific capacitance of 1200 F g⁻¹ at 1 A g⁻¹. It still showed a high capacitance of 1010 F g⁻¹ when current density rose to 5 A g⁻¹, which confirmed the superb rate capability. Yet the cycle stability needs to be further improved for achieving industrial application.

Compliance with ethical standards

Conflict of interest The authors declare that they have no conflict of interest.

References

- Zhang C, Chen Q, Zhan H (2016) Supercapacitors based on reduced graphene oxide nanofibers supported Ni(OH)₂ nanoplates with enhanced electrochemical performance. *ACS Appl Mater Interfaces* 8(35):22977–22987. <https://doi.org/10.1021/acsami.6b05255>
- Fu Y, Song J, Zhu Y, Cao C (2014) High-performance supercapacitor electrode based on amorphous mesoporous Ni(OH)₂ nanoboxes. *J Power Sources* 262:344–348. <https://doi.org/10.1016/j.jpowsour.2014.04.002>
- Jiang C, Zhao B, Cheng J, Li J, Zhang H, Tang Z, Yang J (2015) Hydrothermal synthesis of Ni(OH)₂ nanoflakes on 3D graphene foam for high-performance supercapacitors. *Electrochim Acta* 173:399–407. <https://doi.org/10.1016/j.electacta.2015.05.081>
- Zhan B, Liu C, Chen H, Shi H, Wang L, Chen P, Huang W, Dong X (2014) Free-standing electrochemical electrode based on Ni(OH)₂/3D graphene foam for nonenzymatic glucose detection. *Nanoscale* 6(13):7424–7429. <https://doi.org/10.1039/c4nr01611d>
- Meng T, Ma P-P, Chang J-L, Wang Z-H, Ren T-Z (2014) The electrochemical capacitive behaviors of NiO nanoparticles. *Electrochim Acta* 125:586–592. <https://doi.org/10.1016/j.electacta.2014.01.144>
- Xu L, Chen H, Shu K (2015) Ni(OH)₂/RGO nanosheets constituted 3D structure for high-performance supercapacitors. *J Sol-Gel Sci Technol* 77(2):463–469. <https://doi.org/10.1007/s10971-015-3876-0>
- Sk MM, Yue CY, Ghosh K, Jena RK (2016) Review on advances in porous nanostructured nickel oxides and their composite electrodes for high-performance supercapacitors. *J Power Sources* 308:121–140. <https://doi.org/10.1016/j.jpowsour.2016.01.056>
- Wang B, Chen JS, Wang Z, Madhavi S, Lou XWD (2012) Green synthesis of NiO nanobelts with exceptional pseudo-capacitive properties. *Adv Energy Mater* 2(10):1188–1192. <https://doi.org/10.1002/aenm.201200008>
- Kate RS, Khalate SA, Deokate RJ (2018) Overview of nanostructured metal oxides and pure nickel oxide (NiO) electrodes for supercapacitors: a review. *J Alloys Compd* 734:89–111. <https://doi.org/10.1016/j.jallcom.2017.10.262>
- Zhang W-M, Wu X-L, Hu J-S, Guo Y-G, Wan L-J (2008) Carbon coated Fe₃O₄ nanospindles as a superior anode material for lithium-ion batteries. *Adv Funct Mater* 18(24):3941–3946. <https://doi.org/10.1002/adfm.200801386>
- Liu J, Jiang J, Cheng C, Li H, Zhang J, Gong H, Fan HJ (2011) Co₃O₄ nanowire@MnO₂ ultrathin nanosheet core/shell arrays: a new class of high-performance pseudocapacitive materials. *Adv Mater* 23(18):2076–2081. <https://doi.org/10.1002/adma.201100058>
- Kannan V, Inamdar AI, Pawar SM, Kim HS, Park HC, Kim H, Im H, Chae YS (2016) Facile route to NiO nanostructured electrode grown by oblique angle deposition technique for supercapacitors. *ACS Appl Mater Interfaces* 8(27):17220–17225. <https://doi.org/10.1021/acsami.6b03714>
- Yuan YF, Lin JX, Zhang D, Yin SM, Zhao YL, Yang JL, Chen YB, Guo SY (2017) Freestanding hierarchical NiO/MnO₂ core/shell nanocomposite arrays for high-performance electrochemical energy storage. *Electrochim Acta* 227:303–309. <https://doi.org/10.1016/j.electacta.2017.01.002>
- Hu Q, Gu Z, Zheng X, Zhang X (2016) Three-dimensional Co₃O₄@NiO hierarchical nanowire arrays for solid-state symmetric supercapacitor with enhanced electrochemical performances. *Chem Eng J* 304:223–231. <https://doi.org/10.1016/j.cej.2016.06.097>
- Huang M, Li F, Dong F, Zhang YX, Zhang LL (2015) MnO₂-based nanostructures for high-performance supercapacitors. *J Mater Chem A* 3(43):21380–21423. <https://doi.org/10.1039/c5ta05523g>
- Fei JB, Cui Y, Yan XH, Qi W, Yang Y, Wang KW, He Q, Li JB (2008) Controlled preparation of MnO₂ hierarchical hollow nanostructures and their application in water treatment. *Adv Mater* 20(3):452–456. <https://doi.org/10.1002/adma.200701231>
- Su L, Gao L, Du Q, Hou L, Ma Z, Qin X, Shao G (2018) Construction of NiCo₂O₄@MnO₂ nanosheet arrays for high-performance supercapacitor: highly cross-linked porous heterostructure and worthy electrochemical double-layer capacitance contribution. *J Alloys Compd* 749:900–908. <https://doi.org/10.1016/j.jallcom.2018.03.353>
- Zhu J, Zhang S, Wang D (2017) Facile fabrication of coal-derived activated carbon/Co₃O₄ nanocomposites with superior electrochemical performance. *Ionics* 23(7):1927–1931. <https://doi.org/10.1007/s11581-017-2145-3>
- Wang D, Wang Q, Wang T (2013) Controlled synthesis of porous nickel oxide nanostructures and their electrochemical capacitive behaviors. *Ionics* 19(3):559–570. <https://doi.org/10.1007/s11581-012-0781-1>
- Padmanathan N, Selladurai S, Rahulan K, O'Dwyer C, Razeeb K (2015) NiO hybrid nanoarchitecture-based pseudocapacitor in organic electrolyte with high rate capability and cycle life. *Ionics* 21(9):2623–2631. <https://doi.org/10.1007/s11581-015-1444-9>
- Yadav MS, Tripathi SK (2017) Synthesis and characterization of nanocomposite NiO/activated charcoal electrodes for supercapacitor application. *Ionics* 23(10):2919–2930. <https://doi.org/10.1007/s11581-017-2026-9>
- Chi-Chang Hu K-HC, Lin M-C, Wu Y-T (2006) Design and tailoring of the nanotubular arrayed architecture of hydrous RuO₂ for next generation supercapacitors. *Nano Lett* 6(12):2690–2695
- Zhu Z, Ping J, Huang X, Hu J, Chen Q, Ji X, Banks CE (2011) Hexagonal nickel oxide nanoplate-based electrochemical supercapacitor. *J Mater Sci* 47(1):503–507. <https://doi.org/10.1007/s10853-011-5826-8>
- Cheng G, Yan Y, Chen R (2015) From Ni-based nanoprecursors to NiO nanostructures: morphology-controlled synthesis and structure-dependent electrochemical behavior. *New J Chem* 39(1):676–682. <https://doi.org/10.1039/c4nj01398k>

25. Anandha Babu G, Ravi G, Mahalingam T, Kumaresavanji M, Hayakawa Y (2015) Influence of microwave power on the preparation of NiO nanoflakes for enhanced magnetic and supercapacitor applications. *Dalton Trans* 44(10):4485–4497. <https://doi.org/10.1039/c4dt03483j>
26. Li J, Zhao W, Huang F, Manivannan A, Wu N (2011) Single-crystalline Ni(OH)₂ and NiO nanoplatelet arrays as supercapacitor electrodes. *Nanoscale* 3(12):5103. <https://doi.org/10.1039/c1nr10802f>
27. Liu T, Jiang C, Cheng B, You W, Yu J (2017) Hierarchical flower-like C/NiO composite hollow microspheres and its excellent supercapacitor performance. *J Power Sources* 359:371–378. <https://doi.org/10.1016/j.jpowsour.2017.05.100>
28. Yus J, Ferrari B, Sanchez-Herencia A, Caballero A, Morales J, Gonzalez Z (2017) In situ synthesis and electrophoretic deposition of NiO/Ni core-shell nanoparticles and its application as pseudocapacitor. *Coatings* 7(11). <https://doi.org/10.3390/coatings7110193>
29. Lee JW, Ahn T, Kim JH, Ko JM, Kim J-D (2011) Nanosheets based mesoporous NiO microspherical structures via facile and template-free method for high performance supercapacitors. *Electrochim Acta* 56(13):4849–4857. <https://doi.org/10.1016/j.electacta.2011.02.116>
30. Zhang S, Pang Y, Wang Y, Dong B, Lu S, Li M, Ding S (2018) NiO nanosheets anchored on honeycomb porous carbon derived from wheat husk for symmetric supercapacitor with high performance. *J Alloys Compd* 735:1722–1729. <https://doi.org/10.1016/j.jallcom.2017.11.294>
31. Ren B, Fan M, Liu Q, Wang J, Song D, Bai X (2013) Hollow NiO nanofibers modified by citric acid and the performances as supercapacitor electrode. *Electrochim Acta* 92:197–204. <https://doi.org/10.1016/j.electacta.2013.01.009>
32. Cheng J, Cao G-P, Yang Y-S (2006) Characterization of sol-gel-derived NiO_x xerogels as supercapacitors. *J Power Sources* 159(1): 734–741. <https://doi.org/10.1016/j.jpowsour.2005.07.095>
33. Zhang G, Li W, Xie K, Yu F, Huang H (2013) A one-step and binder-free method to fabricate hierarchical nickel-based supercapacitor electrodes with excellent performance. *Adv Funct Mater* 23(29):3675–3681. <https://doi.org/10.1002/adfm.201203418>
34. Meher SK, Justin P, Rao GR (2011) Nanoscale morphology dependent pseudocapacitance of NiO: influence of intercalating anions during synthesis. *Nanoscale* 3(2):683–692. <https://doi.org/10.1039/c0nr00555j>
35. Cai G, Wang X, Cui M, Darmawan P, Wang J, AL-S E, Lee PS (2015) Electrochromo-supercapacitor based on direct growth of NiO nanoparticles. *Nano Energy* 12:258–267. <https://doi.org/10.1016/j.nanoen.2014.12.031>
36. Yao M, Hu Z, Xu Z, Liu Y, Liu P, Zhang Q (2015) Template synthesis and characterization of nanostructured hierarchical mesoporous ribbon-like NiO as high performance electrode material for supercapacitor. *Electrochim Acta* 158:96–104. <https://doi.org/10.1016/j.electacta.2014.12.058>
37. Cai Y, Ma J, Wang T (2014) Hydrothermal synthesis of α-Ni(OH)₂ and its conversion to NiO with electrochemical properties. *J Alloys Compd* 582:328–333. <https://doi.org/10.1016/j.jallcom.2013.07.206>
38. Meng G, Yang Q, Wu X, Wan P, Li Y, Lei X, Sun X, Liu J (2016) Hierarchical mesoporous NiO nanoarrays with ultrahigh capacitance for aqueous hybrid supercapacitor. *Nano Energy* 30:831–839. <https://doi.org/10.1016/j.nanoen.2016.09.012>
39. Kundu M, Karunakaran G, Kuznetsov D (2017) Green synthesis of NiO nanostructured materials using *Hydrangea paniculata* flower extracts and their efficient application as supercapacitor electrodes. *Powder Technol* 311:132–136. <https://doi.org/10.1016/j.powtec.2017.01.085>
40. Pan S, Chen L, Li Y, Han S, Wang L, Shao G (2018) Disodium citrate-assisted hydrothermal synthesis of V₂O₅ nanowires for high performance supercapacitors. *RSC Adv* 8(6):3213–3217. <https://doi.org/10.1039/c7ra12607g>
41. Li C, Zhang X, Yu P, Zhang H, Sun X, Ma Y (2014) Soft template-assisted synthesis of single crystalline β-cobalt hydroxide with distinct morphologies. *CrystEngComm* 16(32):7478. <https://doi.org/10.1039/c4ce00164h>
42. Ran F, Yang H, Wu Y, Zhao X, Tan Y, Liu Y, Niu X, Chen Y, Kong L, Kang L (2018) Facile preparation of porous nickel oxide membrane for flexible supercapacitors electrode via phase-separation method of polymer. *Mater Res Bull* 103:25–31. <https://doi.org/10.1016/j.materresbull.2018.03.004>
43. Dhole IA, Navale YH, Pawar CS, Navale ST, Patil VB (2018) Physicochemical and supercapacitive properties of electroplated nickel oxide electrode: effect of solution molarity. *J Mater Sci Mater Electron* 29(7):5675–5687. <https://doi.org/10.1007/s10854-018-8537-y>
44. Yuan C, Li J, Hou L, Yang L, Shen L, Zhang X (2012) Facile growth of hexagonal NiO nanoplatelet arrays assembled by mesoporous nanosheets on Ni foam towards high-performance electrochemical capacitors. *Electrochim Acta* 78:532–538. <https://doi.org/10.1016/j.electacta.2012.06.044>
45. Bello A, Makgopa K, Fabiane M, Dodoo-Ahrin D, Ozoemena KI, Manyala N (2013) Chemical adsorption of NiO nanostructures on nickel foam-graphene for supercapacitor applications. *J Mater Sci* 48(19):6707–6712. <https://doi.org/10.1007/s10853-013-7471-x>
46. Xiang D, Liu X, Dong X (2017) A facile synthetic method and electrochemical performances of nickel oxide/carbon fibers composites. *J Mater Sci* 52(13):7709–7718. <https://doi.org/10.1007/s10853-017-1019-4>